EUROfusion

EUROFUSION WP14ER–PR(15)63

O. Février et al.

First Principle Fluid Modelling of Magnetic Island Stabilization by ECCD

Preprint of Paper to be submitted for publication in
Plasma Physics and Controlled Fusion

This work has been carried out within the framework of the EUROfusion Consortium and has received funding from the Euratom research and training programme 2014-2018 under grant agreement No 633053. The views and opinions expressed herein do not necessarily reflect those of the European Commission.

First principle fluid modelling of magnetic island stabilization by ECCD

O. Février[1], P. Maget[1], H. Lütjens[2], J.F. Luciani[2], J. Decker[1,7], G. Giruzzi[1], M. Reich[4], P. Beyer[5], E. Lazzaro[6], S. Nowak[6] and the ASDEX Upgrade team.

[1]CEA, IRFM, F-13108 Saint Paul-lez-Durance, France.
[2]Centre de Physique Théorique, Ecole Polytechnique, CNRS, France.
[3]École Polytechnique Fédérale de Lausanne, CRPP, CH-1015 Lausanne, Switzerland.
[4]Max-Planck-Institut für Plasmaphysik, D-85748 Garching, Germany.
[5]Aix-Marseille Université, CNRS, PIIM UMR 7345, 13397 Marseille Cedex 20, France.
[6]Istituto di Fisica del Plasma P.Caldirola, CNR, Milano, Italy.
[7] Ecole Polytechnique Fédérale de Lausanne (EPFC), Centre de Recherches en Physique des Plasmas, Station 13, CH-1015 Lausanne,Switzerland.

Abstract. Tearing modes are MHD instabilities that reduce the performances of fusion devices. They can however be controlled and suppressed using Electron Cyclotron Current Drive (ECCD) as demonstrated in various tokamaks. In this work, simulations of islands stabilization by ECCD-driven current have been carried out using the toroidal nonlinear 3D full MHD code XTOR-2F, in which a current-source term modeling the ECCD has been implemented. The effiency parameter, η_{RF}, is computed and its variations with respect to source width and location are computed. Influence of parameters such as current intensity, source width and position with respect to the island is evaluated and compared to the Modified Rutherford Equation. We retrieve a good agreement between the simulations and the analytical predictions concerning the variations of control efficiency with source width and position. We also show that the 3D nature of the current source term can lead to the onset of an island if the source term is precisely applied on a rational surface. We report the observation of a flip phenomenon in which the O- and X-Points of the island rapidly switch their position in order for the island to take advantage of the current drive to grow.

1. Introduction

The energy confinement time in tokamaks is a critical issue for achieving the performances required for a fusion reactor. It is however limited by tearing modes that form magnetic islands in the plasma. By locally flattening the pressure profile and acting as a transport short-circuit, these modes limit the maximum achievable $\beta = 2\mu_0 p^2/B^2$ (with p the kinetic pressure and B the magnetic field) and hence the fusion performance. They can however be controlled and suppressed using Radio-Frequence (RF) waves such as Electron Cyclotron Current Drive (ECCD) as demonstrated in various tokamaks, such as AUG[1], DIII-D[2], JT-60U[3], and TCV[4]. Parameters such as the total current injected (and hence the total power required by the ECCD system), the need for precise localization of the mode and current deposition appear to be critical. The width of the current deposition is also an important criterion, as it appears in the figure of merit I_{RF}/δ_I^2 that characterises both the equilibrium [5] and 3D [6] impact of the RF current on the island dynamics. Broad depositions lead to poor efficiency, that must be balanced using, for example, a higher current density and hence a higher injection power. Such criterion criterion will therefore guide the control system for the choice of the orientation of the mirrors of the ECCD system. However, the mechanisms of the mode interaction with the injected current still need to be precised in order to extrapolate present control systems to the next generation of tokamaks, and a first principle modeling is required to go beyond the simplified framework of the Rutherford equation. Previous modeling works have been done in the framework of reduced MHD, with the modeling of the ECRH effect on the m=2 tearing mode [7] and ECCD stabilization [8], both in cylindrical geometries. In the latter work, the RF-driven current density propagates along magnetic field lines in a similar manner to what will be presented in this paper. Modeling in toroidal geometries has also be done in [9] and the effects on equilibrium has been investigated in [10]. These works however differ from the one presented in this paper by the way the current source term is propagated along the magnetic fields lines.

In the present article, we report on the implementation of a RF current source in the 3D full MHD code XTOR-2F, that is then benchmarked against theoretical predictions for the island dynamics. For the first time, the RF efficiency, as described in [6], is compared with analytical predictions. We do recover similar variations with respect to source width, intensity and misalignment to what theory predicts, while a possible role of the island deformation on the overall value of the efficiency is found. The 3D RF source is shown to drive islands, also giving new insights on the flip instability [11] : we observe a fast phase-change of the island O- and X-Points positions through a brief transition of the island's structure to a higher harmonic island.

The article is organized as follows : in a first part, we discuss the model retained for the modeling of the current deposition in the plasma and its homogenization along the magnetic fields lines (section 2). We then briefly describe the analytical model commonly used to model tearing modes stabilization by ECCD (section 3), and describe the one-

fluid MHD model that is employed, as well as the equilibrium that is used as a test case for the numerical simulations (section 4). Then, we report on the simulations using the current source, where we check the influence of parameters such as the width, position and intensity of the current source term. The simulations are compared with the analytical model, showing a good agreement (section 5). In a last section, we discuss two effects that are specific of a 3D localized source term : the first one leading to the onset of a mode if the current source is applied on a rational surface, the second one, known as the flip instability, leading to a rapid switch of the positions of the O- and X-Points (section 6).

2. Current Source

Due to its ability to drive precisely localized current, Electron Cyclotron Current Drive (ECCD) is the method of choice to control tearing modes. The waves launched by the antennas, in a frequency range of about a hundred of GHz, propagate into the plasma where they resonate with the electron cyclotron motion at a precise location. Their power is absorbed and accelerates a population of electrons, that will, by collisions, create an asymmetry in the electron distribution function, hence leading to the apparition of a current. This is known as the Fisch-Boozer mechanism [12]. The associated current density dynamics can be described taking two phenomena into account : The first phenomenom is the homogenization of the current along the magnetic field lines due to the fast flow of the accelerated electrons along those, which can be modeled as a convective propagation of the current density along field lines. A formal derivation can be found in [13], where a two-current model is derived. However, for simplicity purpose, we adopt here a one-current model, which corresponds to one of the asymptotic limits of the model described in [13]. This model is described in equation (2). It gives relatively good results in the limit of slow rotation of the island with respect to the ECCD source term. In case of fast rotating islands, it gives a much less accurate representation of the time evolution of the driven-current density. However, in the simulations presented in this paper, we consider single-fluid MHD simulations with no external momentum sources, hence leading to the validity of retaining this single equation limit. The fast electrons responsible for the RF current will also be subject to radial transport because of collisions and turbulence, leading to the broadening of the current distribution [14]. A perpendicular diffusion term is therefore used to take this phenomena into account. This term can also be used to 'artificially' widen the current source distribution, for instance to simulate the influence of edge density fluctuations which are known to enlarge the ECCD deposition [15]. The second phenomenom is a rise of the generated current, due to the build-up of the asymmetry in the electron distribution function, which occurs on a collisional timescale $\tau_f = \nu_f^{-1}$, where ν_f is the collision frequency of the fast electrons (expressed in equation 1, where ν_{ei} is the thermal ions-electrons collisionality, $\mathrm{v}_{th} = \sqrt{2T_e/m_e}$ the velocity of the thermal electrons and

v_{res} the resonant electrons velocity).

$$\nu_f = \nu_{ei}\left(\frac{\mathrm{v}_{th}}{\mathrm{v}_{res}}\right)^3 \tag{1}$$

For the values considered in the following simulations, τ_f is of the order of a quarter of a millisecond. Finally, these two dynamics can be summarized in a equation (3), which reflects the evolution of the driven current density.

$$\frac{\partial J_{RF}}{\partial t} = \underbrace{\nu_f\left(J_s - J_{RF}\right)}_{\text{Current rise}} + \underbrace{\chi_\perp^{RF}\nabla^2 J_{RF}}_{\text{Broadening}} + \underbrace{\mathrm{v}_{res}\nabla_{||}J_{RF}}_{\text{Homogenization}} \tag{2}$$

The timescale for homogenization along the field lines, τ_h, can be evaluated as in equation (3), where L_H is the length of the considered field line. For convenience, we also express this equation using plasma parameters :

$$\frac{\tau_h}{\tau_A} = \frac{L_H}{v_{res}} \approx 2\pi\frac{v_{th}}{v_{res}}\left(\frac{m_e}{m_i\beta_e}\right)^{\frac{1}{2}}\frac{R_0}{a}\min\left(m, \frac{2\pi}{\sigma_\theta}\right) \tag{3}$$

Where $\beta_e = 2\mu_0 p_e/B^2$ is the electronic beta and σ_θ defines the poloidal extension of the source. This model leads to a rapid homogenization of the current density on the flux surfaces on a time scale of $\tau_h \approx 5\times10^{-4}$ ms for the plasma parameters considered here, where we have set $v_{res}/v_{th} = 2$. However, this advective model appears to be difficult to treat numerically with our code. We therefore show that due to the short time scale of the homogenization compared to the current rise, it can be replaced by a diffusive model, as done in [16] for instance, without changing the physics of RF impact on magnetic islands. This model is shown in equation (4). Note that in this equation, we consider $\chi_{||}^{RF}$ as a free parameter, that we choose so that the homogenization is fast compared to the island dynamics and the current rise. The resulting current density is homogeneous on a flux surface, provided $\chi_{||}^{RF}/\nu_f \ll 1$, as explained in section 2.1.

$$\frac{\partial J_{RF}}{\partial t} = \nu_f\left(J_s - J_{RF}\right) + \chi_\perp^{RF}\nabla^2 J_{RF} + \chi_{||}^{RF}\nabla_{||}^2 J_{RF} \tag{4}$$

2.1. Parallel propagation

In this section, we compare the equilibration timescales of the RF current along the field lines for the two models previously introduced. We consider a gaussian source on a particular field line, defined as

$$J_s = J_s^0 \exp\left(-\frac{(L-L_0)^2}{2\sigma_L^2}\right) \tag{5}$$

where L is the coordinate along the field line. This simple 1D model corresponds to the projection of equations (2) and (4) on a closed field line. For the source term, this gives, using Fourier representation

$$\tilde{J}_s(k) = J_s^0\sqrt{\frac{1}{\sigma_L^2}}\mathrm{e}^{-\frac{1}{2}\sigma_L^2 k^2 + \mathrm{i}L_0 k} \tag{6}$$

When the RF current is established, one has, with the convective model, $v_{\rm res}\nabla_{||}J_{RF} = -\nu_f\left(J_s - J_{RF}\right)$. Using Fourier representation, this gives

$$\tilde{J}_{RF}(k) = \frac{\tilde{J}_s(k)}{1 + i\frac{v_{\rm res}}{\nu_f}\frac{2\pi}{L}k} \tag{7}$$

In our example, this leads to

$$\tilde{J}_{RF}(k) = J_s^0\sqrt{\frac{1}{\sigma_L^2}}\frac{\mathrm{e}^{-\frac{1}{2}\sigma_L^2k^2+\mathrm{i}L_0k}}{1 + i\frac{v_{\rm res}}{\nu_f}\frac{2\pi}{L}k} \tag{8}$$

We can distinguish two asymptotic regimes. If $v_{\rm res}/(L\nu_f) \ll 1$, $\tilde{J}_{RF}(k) \approx \tilde{J}_s(k)$, and the generated current reproduces the source. If $v_{\rm res}/(L\nu_f) \gg 1$, $\tilde{J}_{RF}(k) \approx 0$, except for $k = 0$, where $\tilde{J}_{RF}(0) = \tilde{J}_s(0)$, and therefore, the current is homogeneous on a magnetic field line. This situation is the one encountered for typical plasma parameters. Proceding the same way, one has, for the diffusive model, $\chi_{||}^{RF}\nabla_{||}^2J_{RF} = -\nu_{res}\left(J_s - J_{RF}\right)$ and therefore

$$\tilde{J}_{RF}(k) = J_s^0\sqrt{\frac{1}{\sigma_L^2}}\frac{\mathrm{e}^{-\frac{1}{2}\sigma_L^2k^2+\mathrm{i}L_0k}}{1 + \frac{\chi_{||}}{\nu_f}\left(\frac{2\pi}{L}\right)^2k^2} \tag{9}$$

Again, we have two asymptotic regimes depending on the values of $\chi_{||}^{RF}/(L^2\nu_f)$. If $\chi_{||}^{RF}/(L^2\nu_f) \ll 1$, $\tilde{J}_{RF}(k) \approx \tilde{J}_s(k)$, and the generated current reproduces the source. If $\chi_{||}/\nu_f \gg 1$, $\tilde{J}_{RF}(k) \approx 0$, except for $k = 0$, where $\tilde{J}_{RF}(0) = \tilde{J}_s(0)$, and therefore, the current is homogeneous on a magnetic field line. The figures 1 and 2 show the current distribution along the field line at different time steps, normalized to its final value, for a Gaussian source centered in the middle of the field line, for $L = 2\pi Rm$ with $R = 1.5$ m and $m = 2$, $\nu_{ei} \approx 3.4 \times 10^3$ s^{-1}, $\mathrm{v}_{th} \approx 2.7 \times 10^7$ m.s^{-1}, $\mathrm{v}_{res}/\mathrm{v}_{th} = 2$, and $\chi_{||}^{RF} \approx 2.7 \times 10^7$ m^2.s^{-1}. On a very short timescale, one can see the difference of propagation between the two models (figure 1). Nevertheless, the final current density is almost homogeneous on a field line, and the discrepancy between the two models is small (figure 2). The current density is almost constant along a magnetic field line, equal to the mean value of the current source on this field line.

2.2. Perpendicular propagation

We project equations (2) and (4) on the perpendicular direction, on a radial cord ranging from $\rho \in [-1, 1]$. When the RF current is established, one has $\chi_{\perp}^{RF}\nabla_{\perp}^2J_{RF} = -\nu_{res}\left(J_s - J_{RF}\right)$. We consider the source to be homogenized on the flux surfaces, and therefore, $J_s(\rho) = J_s(-\rho)$. Due to the symmetry of the problem, we then have $J_{RF}(-1) = J_{RF}(1)$ and therefore we treat the problem as being 2-periodic. We therefore can perform Fourier analysis and have, at equilibrium

$$\tilde{J}_{RF}(k) = \frac{\tilde{J}_s(k)}{1 + \frac{\chi_{\perp}^{RF}}{\nu_f}(\pi^2)k^2} \tag{10}$$

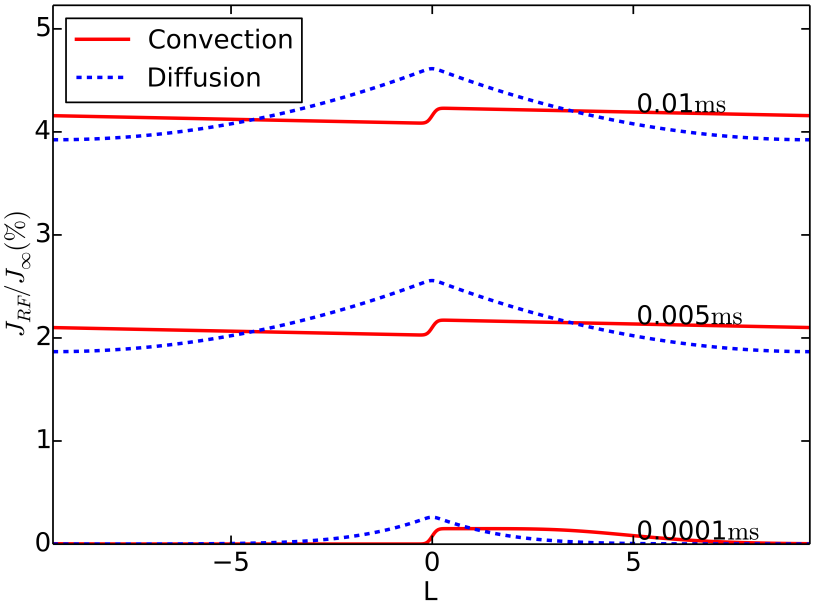

Figure 1. Current density along a magnetic field line, for homogeneization timescale

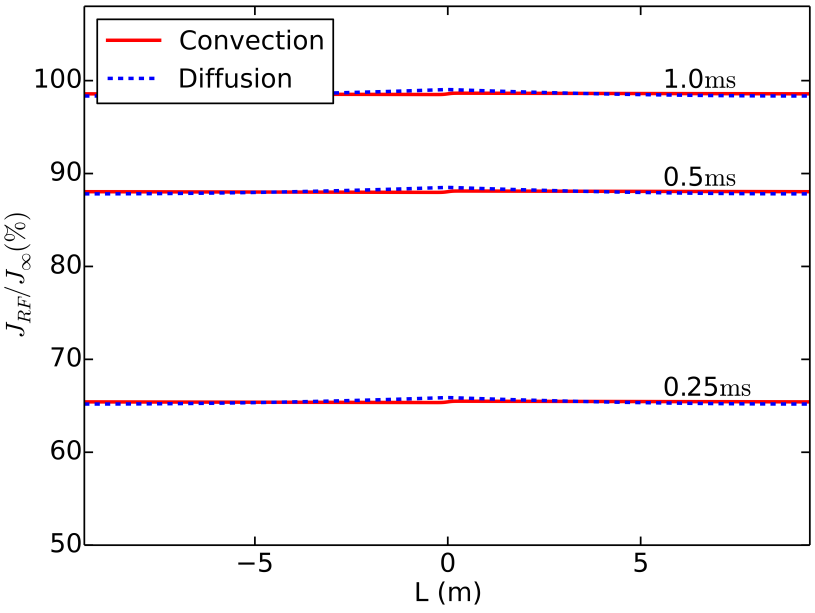

Figure 2. Current density along a magnetic field line, for current-rise timescale

If $\chi_\perp/\nu_f \ll 1$, $\tilde{J}_{RF}(k) \approx \tilde{J}_s(k)$, and the resulting current density is similar to the source in the perpendicular direction, with little to no perpendicular broadening. If $\chi_\perp^{RF}/\nu_f \gg 1$, $\tilde{J}_{RF}(k) \approx 0$, except for $k = 0$, where $\tilde{J}_{RF}(0) = \tilde{J}_s(0)$, and therefore, the current is homogeneous in the perpendicular direction.

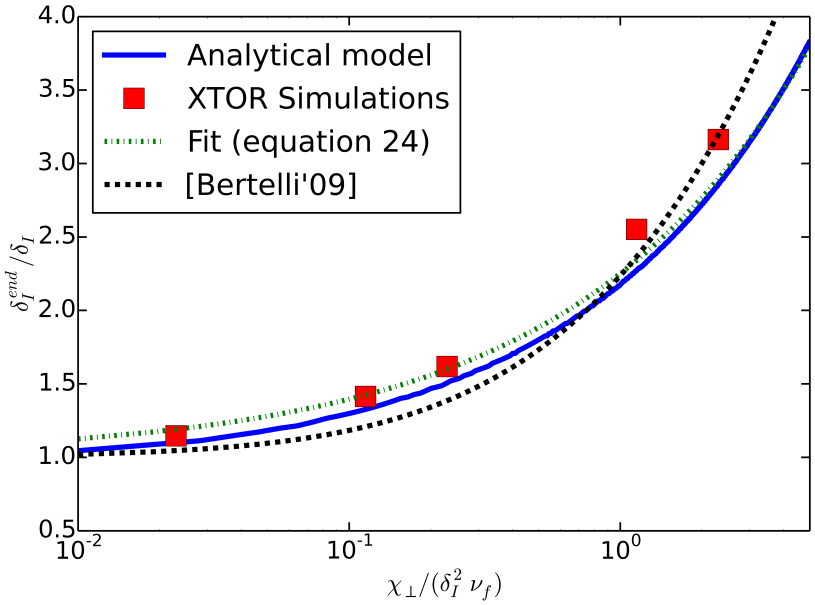

Figure 3. Radial broadening of the initial current distribution due to $\chi_\perp^{RF}$ term in equation (4), for a given source and different values of $\chi_\perp^{RF}$, for the XTOR simulations presented in this article. The fits proposed in equation (12) and the one proposed in [17] are also shown.

3. Modeling of island dynamic

3.1. 3D localized source

The temporal evolution of the island width, here denoted $W = w/a$, can be described by the so-called Generalized Rutherford Equation (GRE) equation. For the classical tearing modes considered in this paper, we can restrain this equation to

$$0.82\tau_R \frac{\mathrm{d}W}{\mathrm{d}t} = a\Delta'(W) + \Delta_{curv} + \Delta_{RF} \tag{11}$$

where $\Delta_{curv} = -6.35\ D_R/\sqrt{W^2 + W_\chi^2}$ accounts for the curvature effects [18]. The expression of W_χ can be found in [19]. Δ', the tearing mode stability index, depends on the island width, especially during the nonlinear stage of its growth. τ_R is the resistive timescale, defined as $\tau_R = \mu_0 a^2/\eta = S\tau_A$ where S is the Lundquist number, τ_A the Alfvén time. The effect of an external current source on the island can be modeled by adding, as done in [6], a term

$$\Delta_{RF} = -\frac{D_{RF}}{W^2}\eta_{RF} \quad \text{with} \quad D_{RF} = \frac{16}{\pi}\frac{\mu_0 R}{s\psi'_s} I_{RF} \tag{12}$$

In this equation, I_{RF} is the total driven current in SI units, $x = \rho_s/a$, where ρ_s is the rational surface position in normalized toroidal flux units, s the magnetic shear, $\psi'_s = \frac{\mathrm{d}\psi}{\mathrm{d}x}$ is the derivative of the poloidal flux on the resonant surface, and η_{RF} a measure of how efficiently the current is used for island stabilization. This efficiency parameter depends

on the source shape and position, as well as on its width compared to the island size, and is defined as

$$\eta_{RF} = \frac{\int \mathrm{d}\Omega \int \frac{\mathrm{d}\alpha}{2\pi} \cos(\mathrm{m}\alpha) \left\langle J_{RF} \right\rangle}{\int \mathrm{d}\Omega \int \frac{\mathrm{d}\alpha}{2\pi} \left\langle J_{RF} \right\rangle} \tag{13}$$

where $\langle \ldots \rangle$ is a flux surface average operator, defined as

$$\langle \ldots \rangle = \frac{\oint \frac{\mathrm{d}\alpha}{2\pi} \frac{\ldots}{\sqrt{\Omega + \cos(\mathrm{m}\alpha)}}}{\oint \frac{\mathrm{d}\alpha}{2\pi} \frac{1}{\sqrt{\Omega + \cos(\mathrm{m}\alpha)}}} \tag{14}$$

Ω is a flux label defined as

$$\Omega = 8 \frac{\left(x - x_s\right)^2}{W^2} - \cos\left(\mathrm{m}\alpha\right) \tag{15}$$

In (equation 15), $\alpha = \theta - \frac{n}{m}\phi$. In this model, the current source is assumed to be perfectly homogenized on the flux surfaces where it is deposed. We have set up a code that evaluates equation (13) after averaging an arbitrary source term over the flux surfaces, using expression 14. On the left panel of figure 5, the efficiency for a source defined as

$$J_s\left(\rho, \alpha\right) = \exp\left(-\frac{\left(\rho - \rho^0_{RF}\right)^2}{2\sigma^2_{\rho_{RF}}} - \frac{\left(\alpha - \alpha^0_{RF}\right)^2}{2\sigma^2_{\alpha_{RF}}} \right) \tag{16}$$

is plotted as a function of the source position (ρ^0_{RF}, α^0_{RF}), while the source width is set to ($\sigma_r = 0.01, \sigma_\alpha = 0.1$). The efficiency is maximum for a source precisely localized on O-Point, and can be destabilizing ($\eta_{RF} < 0$) for a source outside the island or close to its separatrix. The most destabilization location is at the X-Point where ECCD actually destabilizes the island. This can be understood by the fact the the magnetic island can be interpreted as a current filament in the counter-current direction. Therefore, driving co-current in the O-Point counterbalances this filament, hence reducing the island growth. On the contrary, driving current on the X-Point enhances the perturbation induced by the filament and so drives the island growth.

3.2. Rotating island

If the island rotates, and assuming that this rotation is fast enough and is not influenced by the current source, the resulting average efficiency is

$$\overline{\eta_{RF}}\left(\rho\right) = \frac{1}{2\pi} \int_{-\pi}^{\pi} \eta_{RF}\left(\rho, \alpha\right) \mathrm{d}\alpha \tag{17}$$

This result is plotted as the red curve on the right pane of figure 5. It coincides with the efficiency computed for a source term defined as

$$J_s\left(\rho\right) = \exp\left(-\frac{\left(\rho - \rho^0_{RF}\right)^2}{2\sigma^2_{\rho_{RF}}} \right) \tag{18}$$

Therefore, in cases where the island rotates, where the source is fixed, both spatially and temporally (e.g. no modulation) and assuming that the source does not impact much the rotation of the island, we can replace the (ρ, α) localized source by a simple 1D

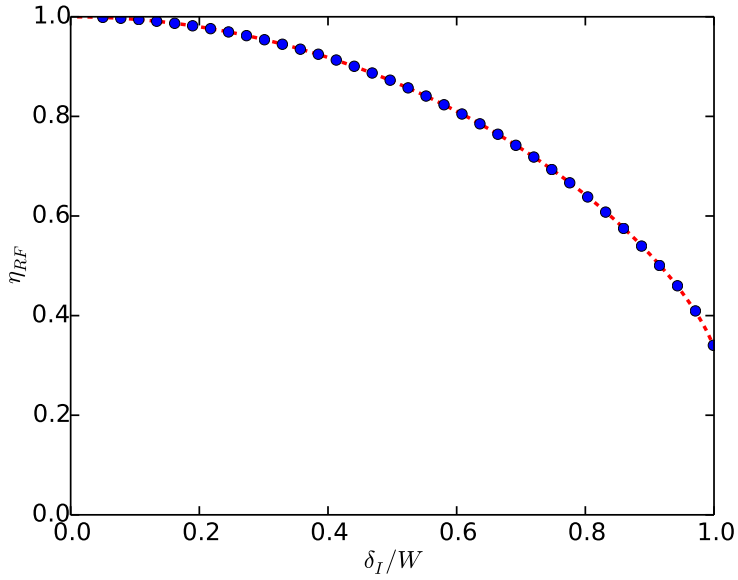

Figure 4. Comparison of η_{RF} computed by direct numerical evaluation of equation 13 and analytical formula, as a function of source width for a Heaviside source profile. The definition of the source term, as well as δ_I and the analytical expression of η_{RF} in this case can be found in [6].

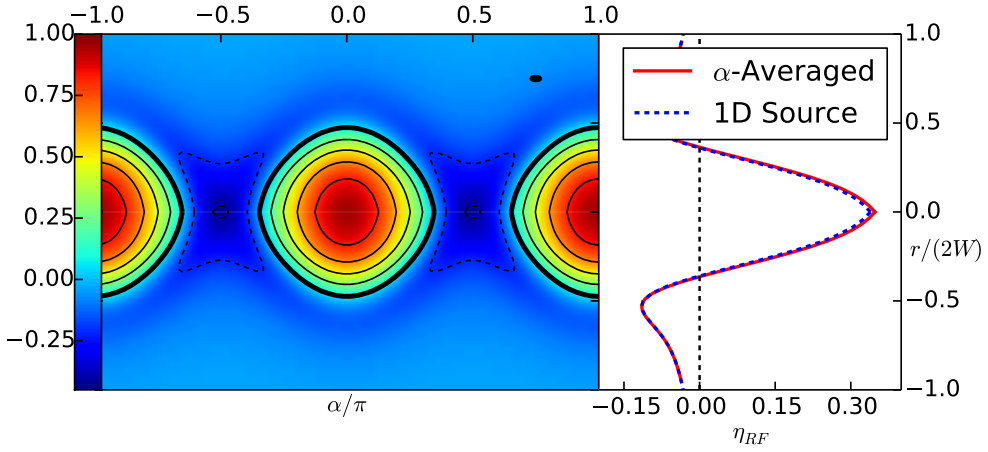

Figure 5. η_{RF} as a function of source position. The black dotted line correspond to contour of negative values.

(r) localized source. This will be relevant for simulations where no momentum source is added, leading to a slower rotation of the mode than in experiments where external momentum sources such as neutral beam injection lead to a fast rotation of the plasma, and hence of the island.

3.3. Effect of misalignment and source width

On figure 6, one can see the evolution of the efficiency of a 1D source depending on its radial width and misalignment. The efficiency is maximum for a narrow current deposition precisely localized on the rational surface. However, it quickly drops with radial misalignment, and can even be destabilizing. With a broader source, the efficiency is smaller, but less sensitive to misalignment. This feature is important for experimental situations, where precise alignment with the flux surface of interest can be difficult to achieve.

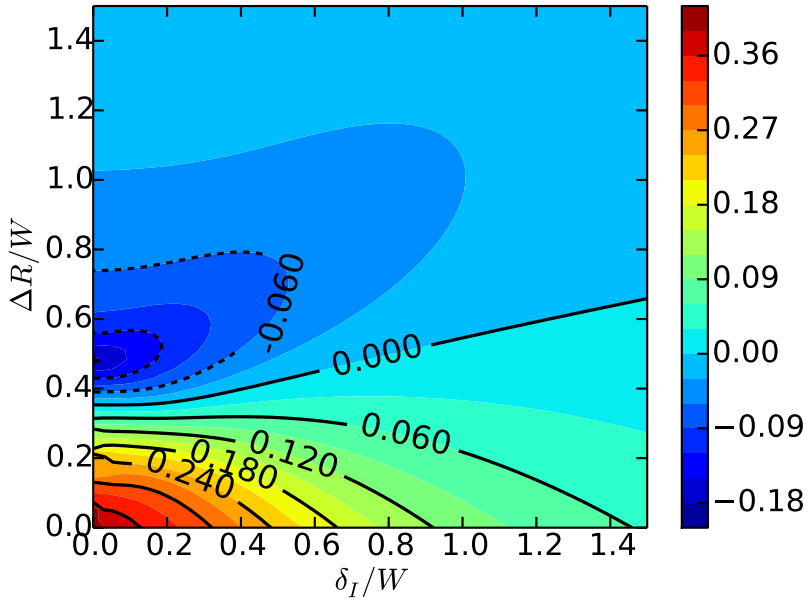

Figure 6. η_{RF} as a function of source width and misalignement. The black dotted line corresponds to contour of negative values.

4. Framework of the simulations

4.1. MHD model

The nonlinear MHD code XTOR-2F [20] solves the two fluid 3D MHD equations in a torus. However, in the framework of this study, we restrict ourselves to a single-fluid case. The equations solved by XTOR are then

$$(\partial_t + \mathbf{V}\cdot\nabla)\, n_i + n_i \nabla\cdot\mathbf{V} + \nabla\cdot\Gamma_{turb} = S \tag{19}$$

$$n_i m_i \left(\partial_t \mathbf{V} + \mathbf{V}\cdot\nabla\mathbf{V}\right) - \mathbf{J}\times\mathbf{B} + \nabla p = \nu\nabla^2\mathbf{V} \tag{20}$$

$$\mathbf{E} + \mathbf{V}\times\mathbf{B} - \eta\left(\mathbf{J} - \mathbf{J_{CD}} - J_{RF}\frac{\mathbf{B}}{|\mathbf{B}|}\right) = 0 \tag{21}$$

$$\partial_t \mathbf{B} = -\nabla\times\mathbf{E} \tag{22}$$

$$(\partial_t + \mathbf{V}\cdot\nabla)\, p + \Gamma p \nabla\cdot\mathbf{V} = \frac{2}{3}\left\{H - \nabla\cdot\mathbf{q}^{\chi}\right\}$$

$$\frac{\partial J_{RF}}{\partial t} = \nu_f \left(J_s - J_{RF}\right) + \chi_{\perp}^{RF} \nabla^2 J_{RF} + \chi_{||}^{RF} \nabla_{||}^2 J_{RF}$$

where $\mathbf{V} = \mathbf{V_E} + \mathbf{V_{||i}}$. $\mathbf{J_{CD}}$, defined as $\mathbf{J_{CD}} = \mathbf{J}|_{t=0}$, is a current source intended to restore the equilibrium current profile. The ratio of specific heat is $\Gamma = 5/3$, H is the heat source, destined to restore equilibrium pressure profile and $q^{\chi} = -\rho\chi_{||}\nabla_{||}T - \rho\chi_{\perp}\nabla_{\perp}T$ is the heat flux, with $T = p/\rho$ and $\chi_{||}$ and $\chi_{\perp}$ diffusion coefficients accounting for the parallel and perpendicular transport. $\chi_{\perp}$ models both the collisional and turbulent radial transports. S is a particle source used to restore density profile. The turbulent-induced particles transport is modeled by a flux $\Gamma_{turb} = -D_{\perp}\nabla\rho$ where $D_{\perp} = \frac{2}{3}\chi_{\perp}$. The current induced by the RF source is implemented as a parallel term $\mathbf{J_{RF}} = J_{RF}\frac{\mathbf{B}}{|\mathbf{B}|}$ in the Ohm's law, where the time evolution of the term J_{RF} is handled by the models discussed in section 2.

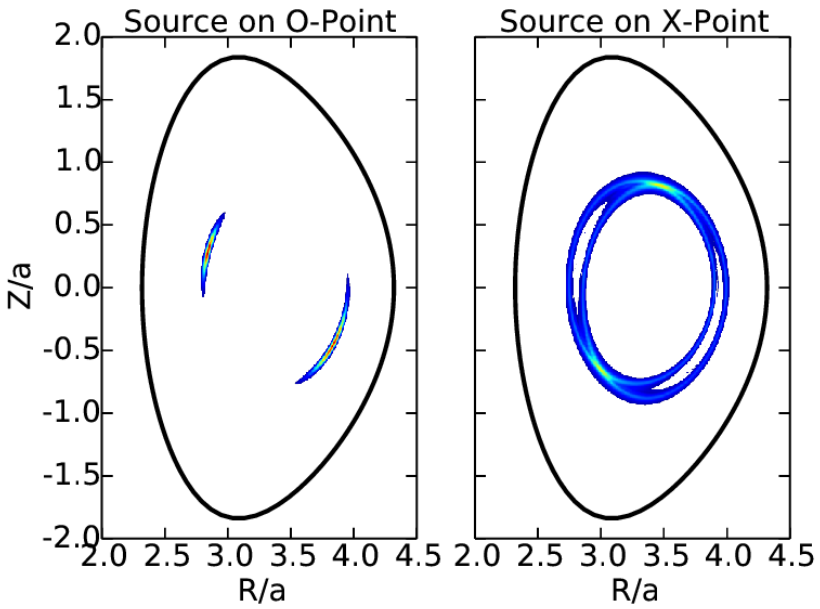

Figure 7. Propagation of the RF current on the flux surfaces, depending on the initial localization of the source in presence of a (2,1) island. For the purpose of this figure, a thin source ($\sigma_r = 0.01$, $\sigma_\theta = 0.05$ and $\sigma_\phi = 0.25$) as well as a low $\chi_{\perp}^{RF}$ ($\chi_{\perp}^{RF}/\eta = 75$) have been used.

4.2. Equilibrium and current source

For demonstration purpose, we use an ASDEX-Upgrade-like equilibrium in the presented simulations. For simplicity, the shape of the separatrix is modified to be up-down symmetric, and there is no X-Point. Pressure and density profiles are fitted from AUG pulse #29682 (figure 8). The central ion density is $n_i^0 = 8.2 \times 10^{19}$ m^{-3} while the magnetic field on the axis is $B_0 = 2.65$ T. The pressure is artificially reduced so as to deal with linearly unstable tearing modes. Indeed, tearing modes are efficiently stabilized by curvature effect [21], with an effective Δ' that decreases linearly with β [22].

The figure 9 shows the evolution of linear growth rate of the (2,1) mode with respect to β_N. This mode is unstable for $\beta_N < 1.2$. The original equilibrium has $\beta_N \approx 2$, and therefore tearing modes are linearly stabilized by the curvature. We therefore reduce the pressure by a factor 3, in order to reach $\beta_N \approx 0.7$, for which the (2,1)-mode is unstable. At saturation, we observe a large $(2,1)$-mode, whose size is $W_{sat} \approx 0.11$, expressed in square root of the normalized (to the value on separatrix) poloidal flux unit, $r = \sqrt{\psi}$, and also $W_{sat} \approx 0.11$ expressed in normalized toroidal flux units. The surface $q = 2$ is located on $r_s = \sqrt{\psi_s} = 0.68$, corresponding to $x = \rho_s/a = 0.5098$. $\chi_\perp$, the perpendicular diffusion coefficient of the thermal particles is chosen such that $\mu_0\chi_\perp/\eta = 150$, and $\chi_{||}$ is chosen such that $\chi_{||}/\chi_\perp = 10^8$. The Lundquist number is $S = 10^7$. The central Alfvén time is $\tau_A = 3.61 \times 10^{-7}$ s, and the ratio between the real resistivity and the resistivity used in the code is $S^{real}/S^{XTOR} \approx 16$. The time is therefore rescaled as $t^{real} = \tau_A \left(S^{real}/S^{XTOR}\right) t^{XTOR}$. The current source term J_s that appears in equation (23) is defined as

$$J_s\left(r,\theta,\phi\right) = J_s^0 \exp\left(-\frac{(r-r_{RF}^0)^2}{2\sigma_{r_{RF}}^2} - \frac{(\theta-\theta_{RF}^0)^2}{2\sigma_{\theta_{RF}}^2} - \frac{(\phi-\phi_{RF}^0)^2}{2\sigma_{\phi_{RF}}^2}\right) \tag{23}$$

The source width δ_I is the radial full width at half maximum of the source and is defined as $\delta_I = 2\sqrt{2\ln 2}\sigma_{r_{RF}}$. Figure 7 shows the propagation a current source along the whole flux surface, in the presence of a $(2,1)$ island. The source term is chosen as a thin gaussian ($\sigma_{r_{RF}} = 0.01$, $\sigma_{\theta_{RF}} = 0.1$ and $\sigma_{\phi_{RF}} = 0.25$) which is centered in the island's O-Point on the left panel. It will propagate along the field line thanks to the $\chi_{||}^{RF}$ term. On right panel is plotted the opposite situation, where the source term is centered precisely on an X-Point of this island. Since it lies on the rational surface ($q = 2$), it will propagate and form a (2,1)-current filament. Transverse diffusion as well as non-null value of the source's width allow propagation on the whole flux surface.

4.3. Impact of parallel homogenization and perpendicular diffusion on island dynamics

For numerical reasons, we use the diffusive model (equation 4) to simulate the establishment of the current. On figure 10 are plotted the initial variations of the island size for different values of the parallel diffusivity. For sufficiently large values of $\chi_{||}^{RF}$, there is no notable difference on the island decay behavior : in these cases, the current is almost perfectly homogenized on the flux surfaces, and increasing $\chi_{||}^{RF}$ has no further effect. On figure 3, the results obtained with the model implemented in XTOR equations (4) are plotted and compared to the curve obtained with this simple analytical model, for a Gaussian source of width δ_I. As one can see, the broadening of the ECCD current density due to the perpendicular diffusion implemented in XTOR behaves as expected. It can simply be fitted by

$$\frac{\delta_I^{end}}{\delta_I} = 1 + \frac{1.25}{\delta_I}\sqrt{\frac{\chi_\perp^{RF}}{\nu_f}} \tag{24}$$

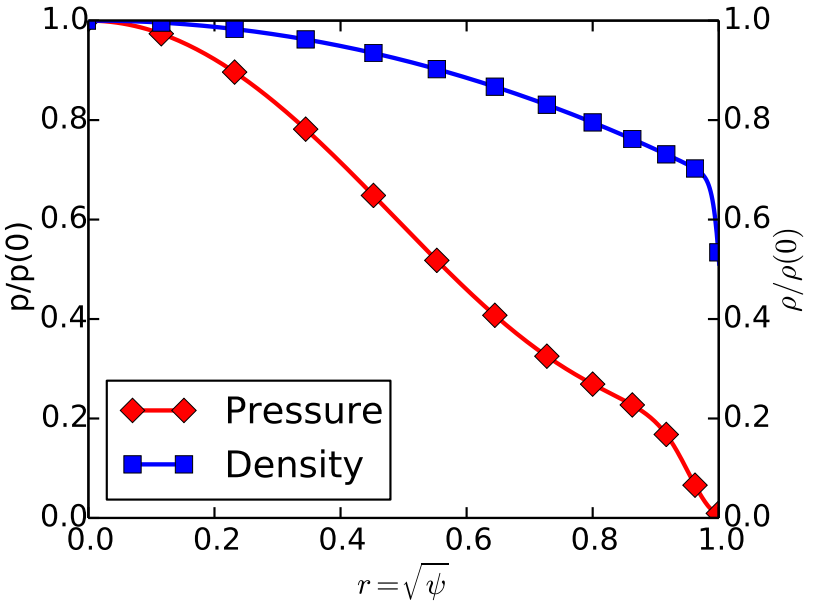

Figure 8. Pressure and density profiles used in the simulations.

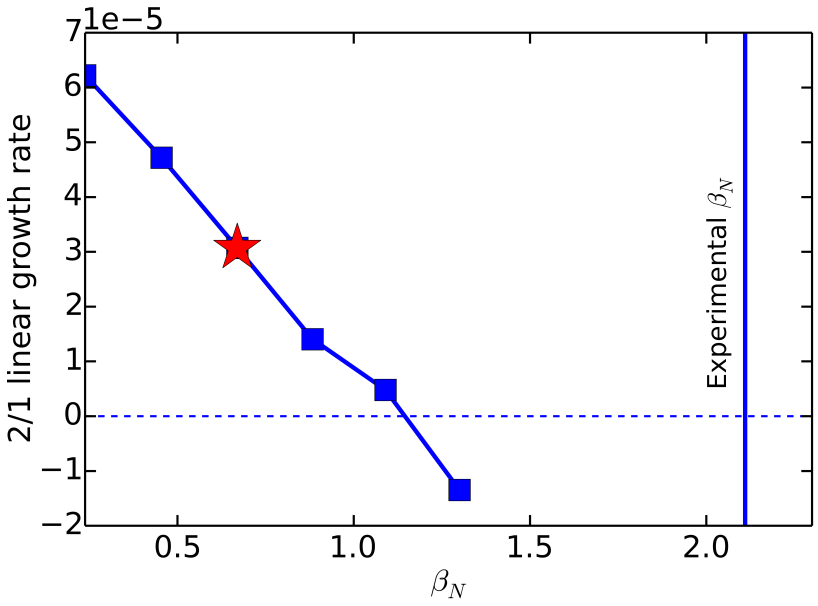

Figure 9. Evolution of the (2,1)-tearing mode growth rate with β_N. The red star shows the reduced pressure case that has been chosen in the study.

Another fit, proposed in [17], is also plotted on figure 3 :

$$\frac{\delta_I^{end}}{\delta_I} = \sqrt{1 + 4\frac{\chi_\perp^{RF}}{\nu_f}} \tag{25}$$

The broadening of the source resulting from this perpendicular diffusion will lead to a decrease of the control efficiency. In typical simulations where the perpendicular diffusion coefficient of the thermal particles is used as a value for $\chi_\perp^{RF}$, we have

$\chi_{\perp}^{RF}/\nu_f \approx 1 \times 10^{-3}$

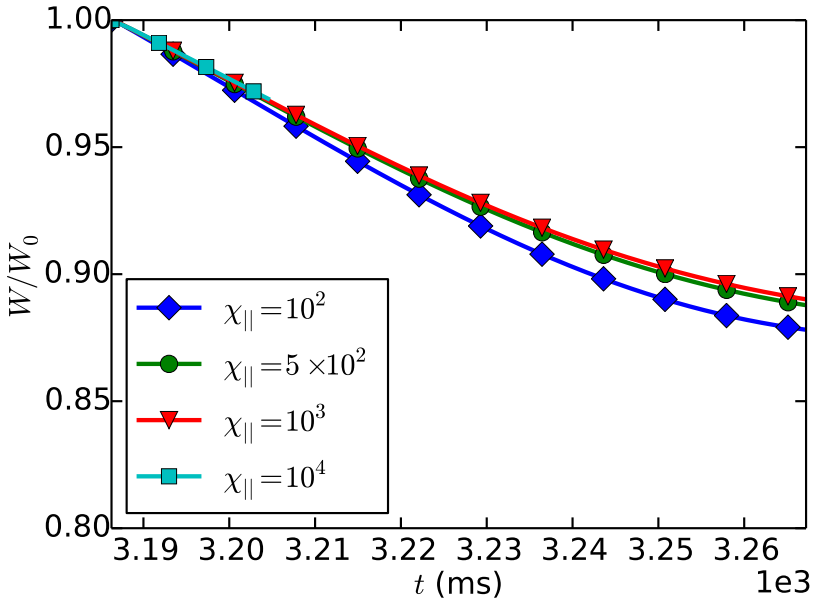

Figure 10. Initial island decay under the influence of an external 3D current source as defined in equation (23), for different values of $\chi_{||}^{RF}$, for the XTOR simulations presented in this article. Above a certain value of $\chi_{||}^{RF}$ the evolution is similar.

5. The RF efficiency: prediction and numerical results

In this section, we focus on the evaluation of the RF efficiency, with a comparison of numerical results with theoretical predictions.

5.1. Methodology

Using equation (11), one has, at saturation, $\frac{\mathrm{d}W}{\mathrm{d}t} = 0$, and therefore, when the RF source term is switched on at $t = t_{RF}$, one has

$$\left[\left.\frac{\mathrm{d}W}{\mathrm{d}t}\right|_{t=t_{RF^+}} - \left.\frac{\mathrm{d}W}{\mathrm{d}t}\right|_{t=t_{RF^-}} \right] = -\frac{D_{RF}}{W_{sat}^2}\eta_{RF}(W_{sat}) \tag{26}$$

This jump of the island width derivative can be measured using simulations data, as shown on figure 12. As pointed out in (equation 26), the value of this jump can directly be linked to the value of $\eta_{RF}(W_{sat})$. Note that the term ψ', that intervenes in equation 12, must be properly evaluated from the toroidal equilibrium : the cylindrical approximation $\psi' = a^2 x B_0/q$ is significantly lower and would lead to an underestimation of η_{RF} in case of non-circular and toroidal geometry, as plotted on figure 11.

During the simulations, the source positions θ_{RF}^0 and ϕ_{RF}^0 are chosen such that the peak of the gaussian is inside the O-Point of the island. The source dimensions $\sigma_\theta = 0.15$ rad, and $\sigma_\phi = 0.4$ rad, are fixed. We vary the width of the current deposition

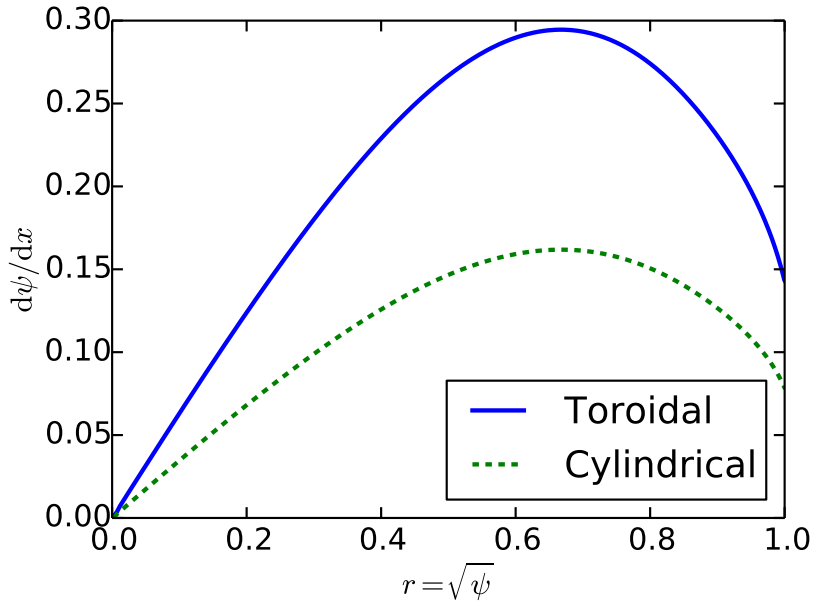

Figure 11. Evaluation of ψ' in toroidal case, and with a simple cylindrical expression $\psi' \approx a^2 x B_0/q$

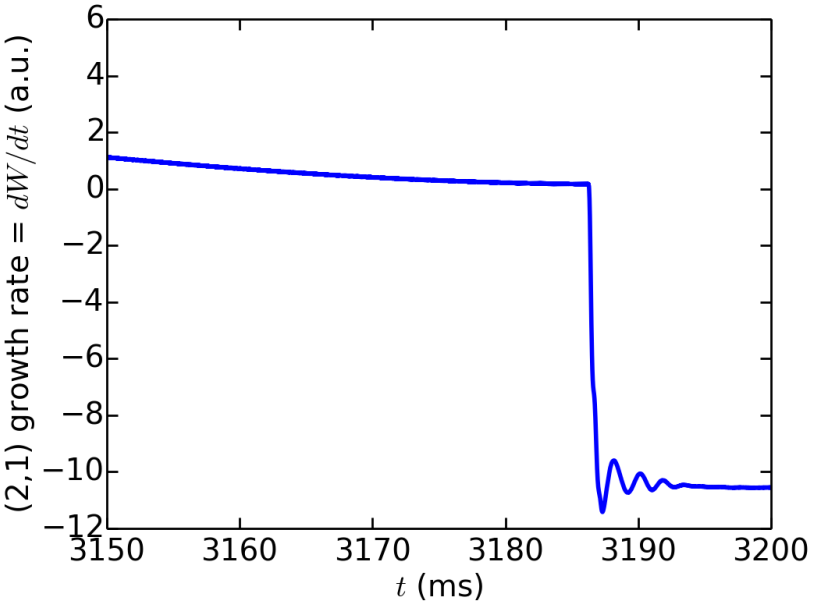

Figure 12. Jump in the island's width derivative when RF-driven current is applied, at $t \approx 3186$ ms.

(by varying σ_r), keeping a constant total driven current $I_{RF} \approx 5.9kA$. On figure 13, the efficiency obtained is shown. One can see that the efficiency computed with XTOR is lower than expected from the theory. Simulations with a circular cross-section (not shown here) do not exhibit this difference. This result has been checked with higher poloidal and toroidal resolutions, leading to the same computed efficiency.

On top panel of figure 14 is plotted the island obtained with a circular equilibrium, as well a fit using analytical expression used in [23]. On the bottom panel of figure 14, the island obtained for the elongated plasma case is plotted. This suggests a possible role of the island deformation, which can indeed modify the RF efficiency [24, 23, 25]. The radial shift of the O-point (parameter $\epsilon \sim -1$ in the notations of [23]) and the inside/outside asymmetry (parameter $\gamma \sim 1$) are quite large in both the circular and elongated plasma cases. The poloidal deformation of the island, combined with these radial deformations, might be at the origin of this change between circular and elongated plasma shapes. Another possibility is the fact that the source shape is defined using the geometric θ angle in the poloidal direction, while the island shape should be considered using the intrinsic poloidal angle θ^*.

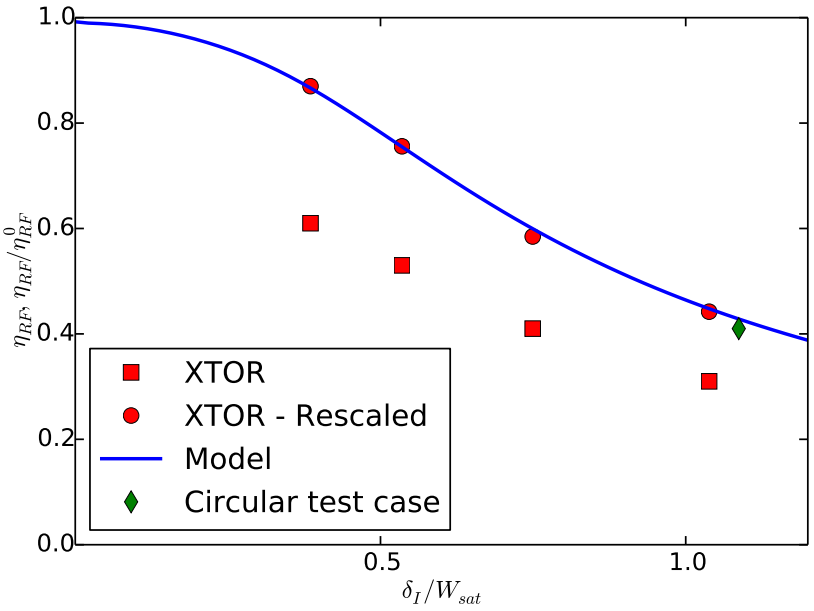

Figure 13. Variation of the efficiency η_{RF} with respect to the source radial size, as computed in XTOR simulations, and using analytical model developed by Hegna, as expressed in equation (13). The circles correpond to the values used to plot the square series, rescaled by a constant (common to all the points) so that they lie on the analytical curve.

5.2. Relative comparaison of XTOR simulations with Rutherford equation

In this part, we consider that the efficiency η_{RF} can be written as $\eta_{RF} = \eta^0_{RF} F_1(\delta_I/W) F_2(\Delta r/W)...$, where F_1, F_2, etc. are form factors characterizing the evolution of η_{RF} for the relevant parameters of the problem. We have seen in the previous section that the efficiency computed with XTOR is lower than predicted by the Rutherford theory. Therefore, in order to compare the Rutherford equation and the simulations, we rescale the efficiency obtained with XTOR by the factor η^0_{RF} found in the previous section.

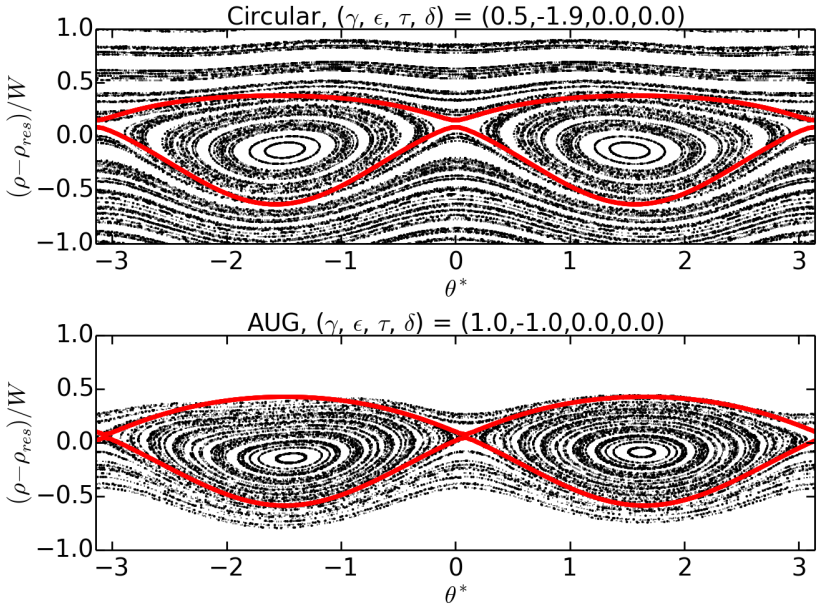

Figure 14. Comparison of the island shapes for a circular test case and the elongated AUG equilibrium, where θ^* is the intrinsic poloidal angle

5.2.1. Effect of total current injected and source width on island decay rate. Investigating the impact of current density on island stabilization is crucial, as it is directly linked to the total power required by the ECCD system, that one would like to minimize in a fusion reactor. The definition of D_{RF} (equation 12) shows that $\frac{\mathrm{d}W}{\mathrm{d}t}\Big|_{t=0^+}$ depends linearly on I_{RF}. As shown on figure 15, we retrieve this behavior within our simulations. The data from figure 13 are then plotted on 16, but rescaled with the effiency factor η^0_{RF}. As one can see, the form factor $F_1(\delta_I/W)$ is very similar for the different curves and in good agreement with what is expected from the theory. The behavior observed in XTOR is in good agreement with the equation (13), computed for a Gaussian source term, defined as in equation (16). A good fit can be proposed in the spirit of what is suggested in [2], by using

$$F_1(\delta_I/W) = \frac{\eta_{RF}}{\eta^0_{RF}} = \frac{1}{1+(\delta_I/W)^2} \tag{27}$$

5.2.2. Effect of misalignment This alignment of the RF-current deposition with the radial position of the mode is known to be a critical issue. Best efficiencies are obtained for a deposition centered on the island O-Point, while deposition close to the island separatrix can lead to island destabilization. However, it might be experimentally difficult to locate precisely the resonant surface of interest. Even if a precise determination of the mode radial position was possible, orienting the ECCD system to deliver current exactly on the mode can be difficult to achieve. It is therefore necessary to assess the impact of misalignment on island evolution [26] [27]. In the following simulations, we vary the position of the source around the surface r_s, its width

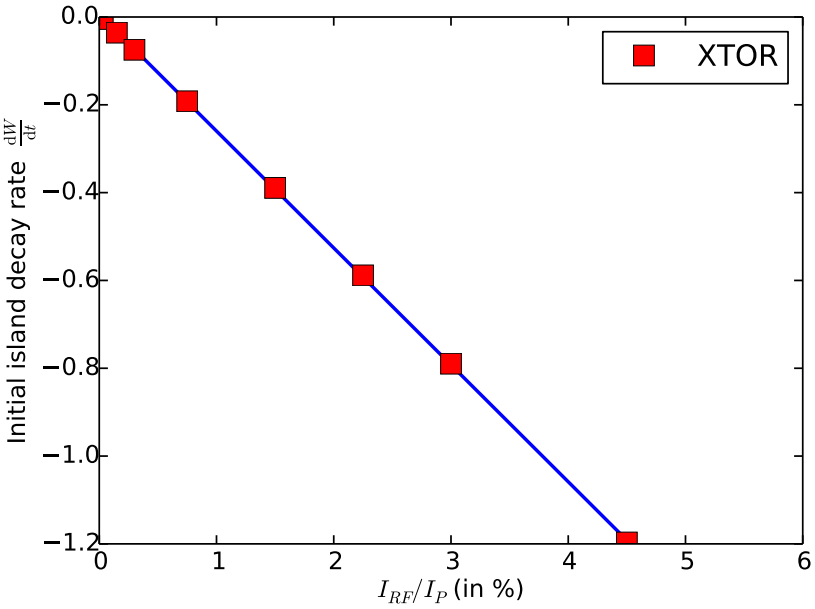

Figure 15. Variation of the initial decay rate of the island's size with respect to the total current, I_{RF}, injected into the island.

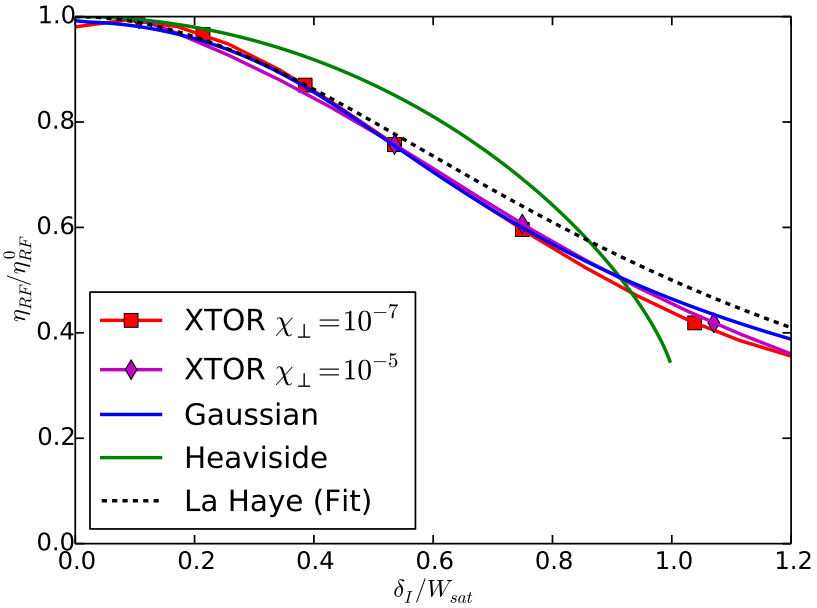

Figure 16. Variation of the efficiency η_{RF} with respect to the source radial size, as computed in XTOR simulations, and using analytical model developed by Hegna, as expressed in equation (13).

being held constant. The figure 18 shows the comparison of the results obtained with the XTOR simulations and the analytical computation. The efficiency is maximum when the source hits the O-point, at a radial position r_O that is inside the resonant surface position r_s. Since in our analytical model, it is assumed that $r_s = r_O$, on figure 18, we

have shifted the curve corresponding to the Hegna's model so that its origin is on r_O and not on r_s. For radial positions inside the island, we retrieve the stabilization suggested by the computation of η_{RF}. The shape of the curve obtained is also consistent with the results obtained by Perkins in [28]. We however observe an asymmetry, which is not present in the analytical model we used to compute the efficiency. This asymmetry is due to the asymmetry of the shape of the island (see figure 17), which is consistent with [23]. A relatively good fit, though it does not exhibit the asymmetry, can be suggested in the spirit of what is proposed in [27] using experimental data. This fit is plotted on figure 18, and corresponds to ($\Delta_r = r^0_{RF} - r_s$)

$$F_2\left(\frac{\Delta r}{W}\right) = \frac{\eta_{RF}}{\eta^0_{RF}} \propto \exp\left(-\left(\frac{5}{3}\frac{2\Delta r}{W_{sat}}\right)^2\right) \tag{28}$$

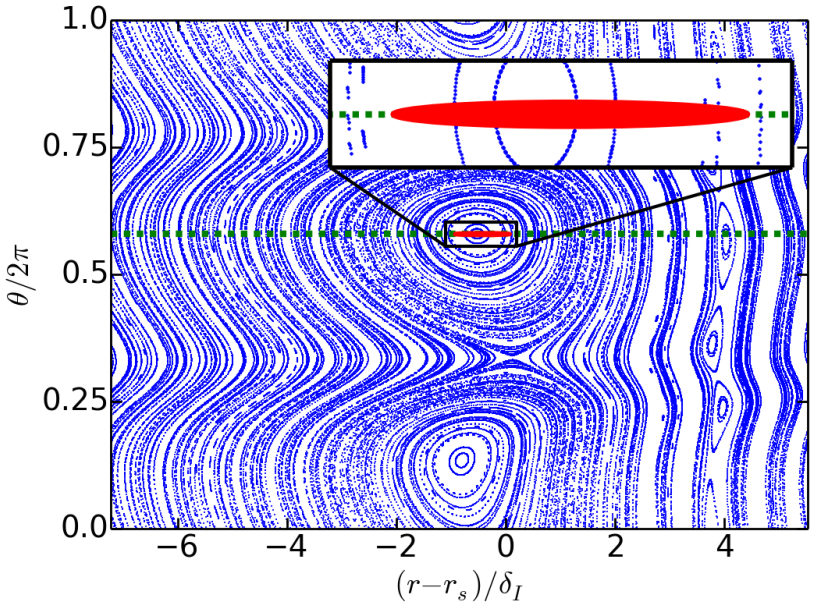

Figure 17. Poincaré plot of the island. The red ellipse shows the radial and poloidal extension of the current source.

6. Effect of 3D localization of the source on island dynamics

In this section, we study the long-time response of the plasma to a 3D localized current source term, in the absence of plasma rotation. As shown in the following subsections, the island arranges itself in a situation where the current perturbation induced by the source is favorable to its growth. In the case of a well localized current deposition on an equilibrium, this means that an island will be generated, while injecting current on an already existing island can lead to a phase shift of the latter in order to favor its growth. We show that when the plasma and/or the islands rotats, these effects disappear as they come from the fact that in a non-rotating plasma, driving a continuous current at a fixed

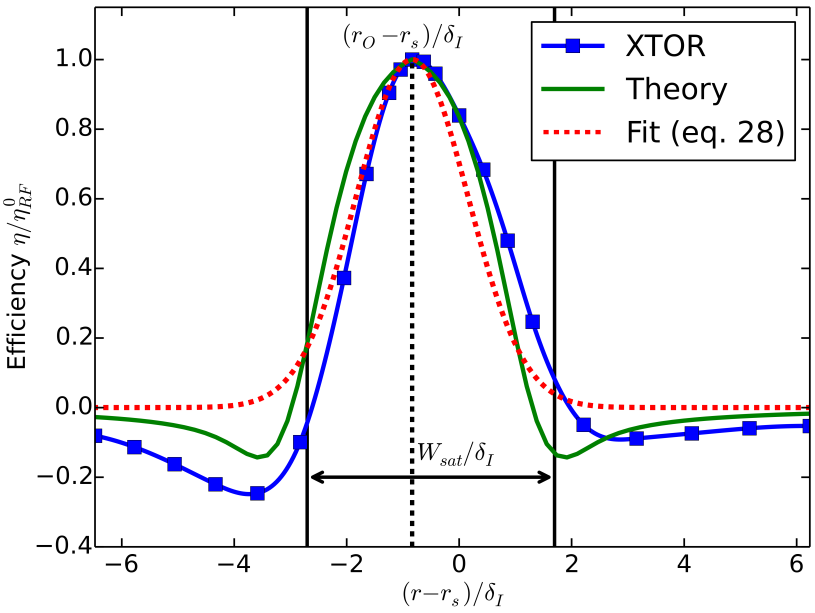

Figure 18. Variation of the efficiency η_{RF} with respect to source misalignment with resonant surface.

position creates a privilieged point for the island growth or flip. When the plasma or the island rotates, there is no priviliged point anymore.

6.1. Mode onset by ECCD

In this subsection, we consider the equilibrium described in 4.2, except that we do not reduce the pressure, and therefore tearing modes are stable. We drive current on the rational surface $q = 2$ in the form of a narrow source ($\sigma_r = 10^{-3}$, $\sigma_\theta = 10^{-1}$ and $\sigma_\phi = 10^{-1}$). In a first case, the source is only defined as a 1D source such that $J_s = J_s(\sqrt{\psi})$, corresponding to the case where the current is homogeneous on the equilibrium flux surfaces. In that case, we do not observe the onset of a mode. If however we define the source term as a 3D localized source term, its propagation along field line creates a current filament with the helicity of the rational surface, hence generating an island. However, due to the finite extension of the source in the poloidal and radial directions, even a very-well localized source term on a resonant surface will tend to homogenize on the flux surface. Therefore, for ECCD to be able to drive a magnetic island, it is necessary that the characteristic time of the current equilibration along a magnetic surface is longer than the time needed to create the island from the current filament, so that the 3D effects and current inhomogeneity along magnetic surface can have an impact. The figure 19 shows the evolution of the (2,1) island width for the case with a 1D and a 3D RF source centered on the resonant surface $q = 2$. On figure 20, the size of the resulting island is plotted with respect to the source position compared to the resonance. As one can see, well localized ECCD deposition can generate an island on the vicinity of the resonant layer. Finally, the size of the resulting island is

plotted against the total current injected with the source, expressed as a percentage of the plasma current (figure 21).

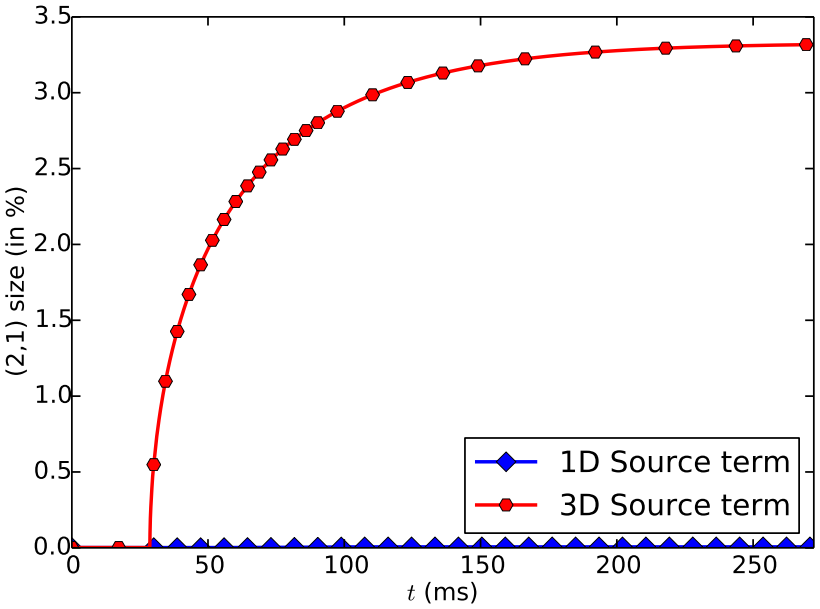

Figure 19. Energy of the (2,1) mode depending on the shape of the current source term ($I_{RF}/I_P = 0.75\%$).

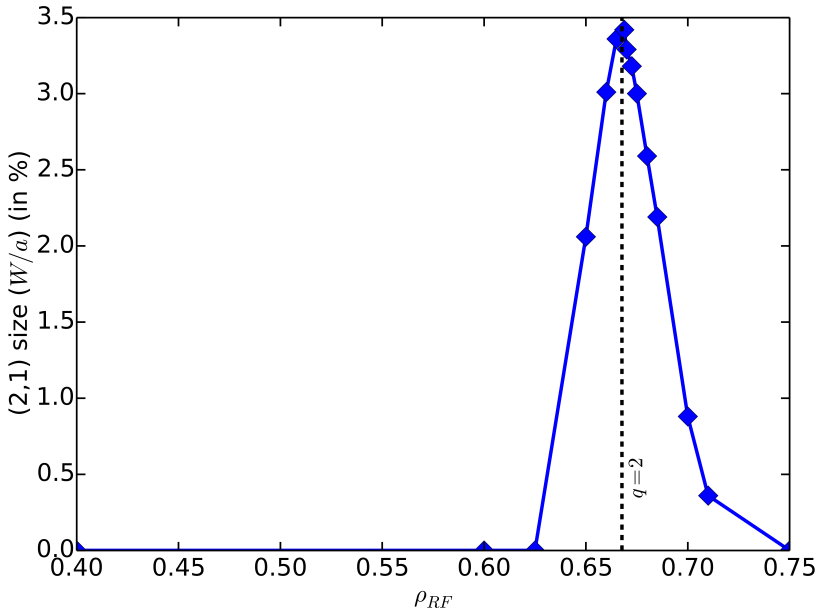

Figure 20. Size of the (2,1) mode depending on the radial position of the 3D current source ($I_{RF}/I_p = 0.75\%$, $\delta_I = 2.36 \times 10^{-3}$).

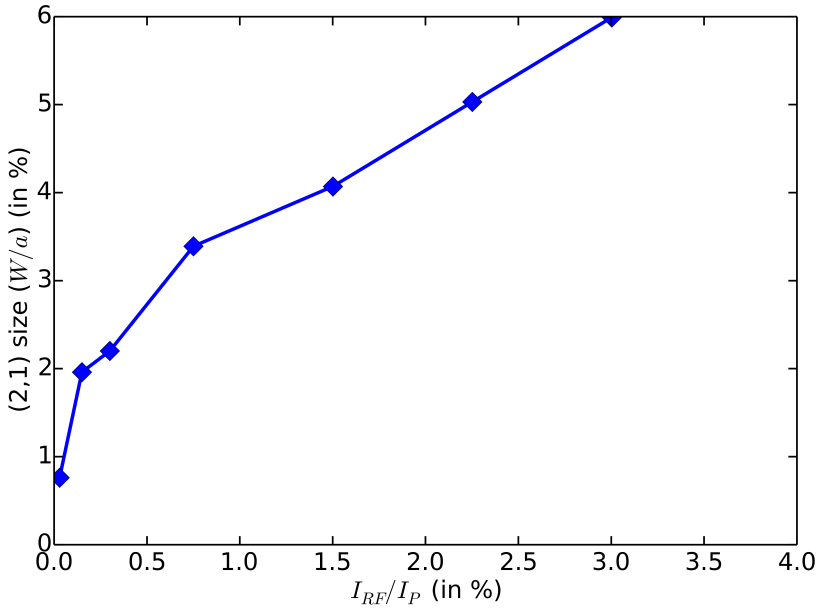

Figure 21. Width of the (2,1) mode depending on the total injected current ($\delta_I = 2.36 \times 10^{-3}$).

6.2. Flip instability

We now come back to the low β_N cases with a large saturated (2,1) island. In the presence of a 3D localized source, applied such that at the initial time, it lies in the O-point of the island, we observe, after a phase of decrease of the island size, an abrupt change of the phase of the island in a few tens of milliseconds, so that the source is now localized close to an X-point, leading to the growth of the island. This is depicted on figure 22, where the evolution of the size of the island is plotted for several value of the total injected current. The figure 23 shows the evolution of the X-point poloidal position (θ-angle) during this process. First, the two X-points of the $(2,1)$-mode move steadily, until the mode is reduced enough so that the $(4,2)$-mode dominates. The source, initially located on an O-point of the (2,1) mode, is now located on one of the X-Points of this mode, which leads to the regrowth of the $(2,1)$-mode, whose X and O-points have switched positions. Observing the Poincare maps of the magnetic field (figure 24) during the flipping period reveals that this phenomenon is not linked to a rotation of the mode, but to a change of its structure and phase. We also observe that after this process, the mode appears to be locked in a certain position, as O and X-points locations stop to evolve. The figure 23 shows the final position of the island X-points with respect to the source position. The source is in an intermediate position between the O-point and the X-point, where the efficiency η_{RF} is negative, hence leading to the growth of the mode. This flip occurs on a 50 ms timescale (figure 25). This instability is described in [11], where it is referred as the "flip" instability. A similar behavior can be observed when applying a magnetic perturbation (such as RMP) to an island, where in some cases, the island will lock in a particular phase with respect to the applied

perturbation [29]. It should be noted that adding further harmonics in the simulation does not change significantly the flip behavior.

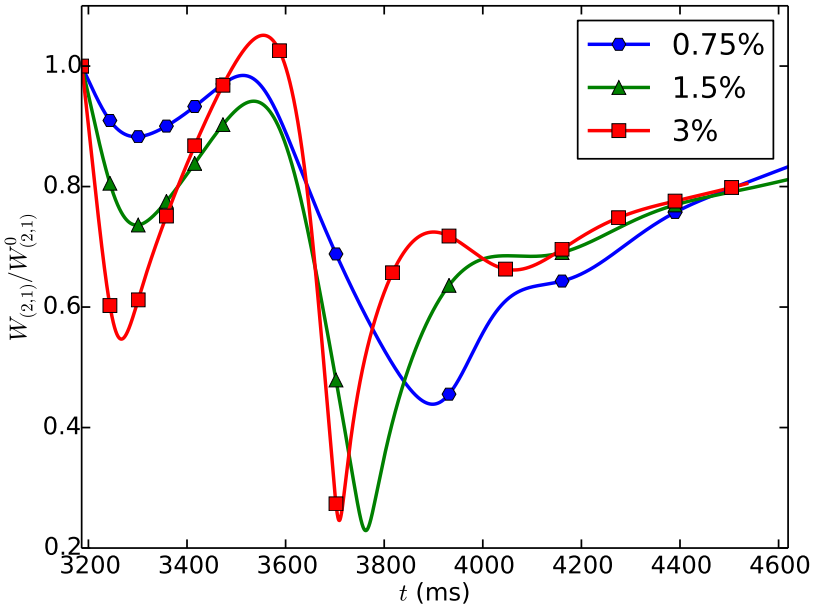

Figure 22. Evolution of the size of the $W_{(2,1)}$ island for different values of the total injected current.

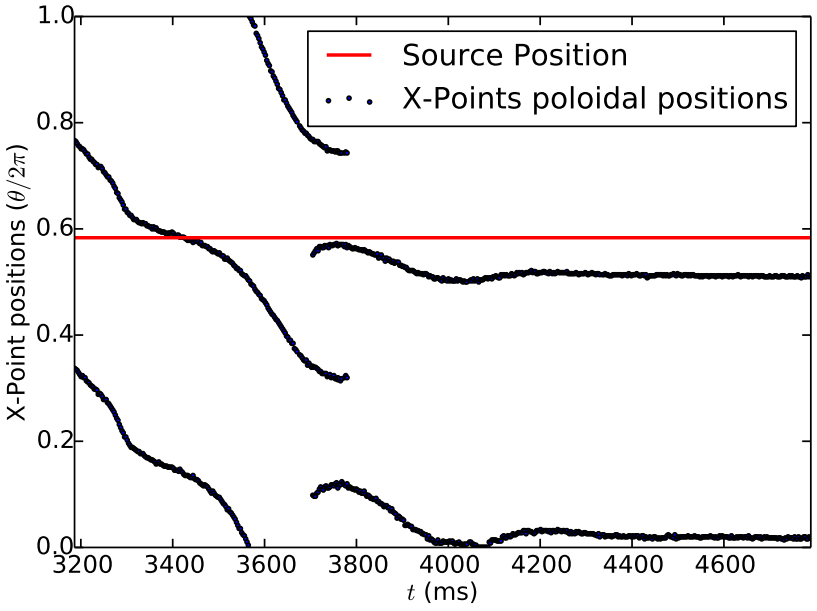

Figure 23. Evolution of the X-points poloidal position evolution, for $I_{RF}/I_P = 1.5\%$.

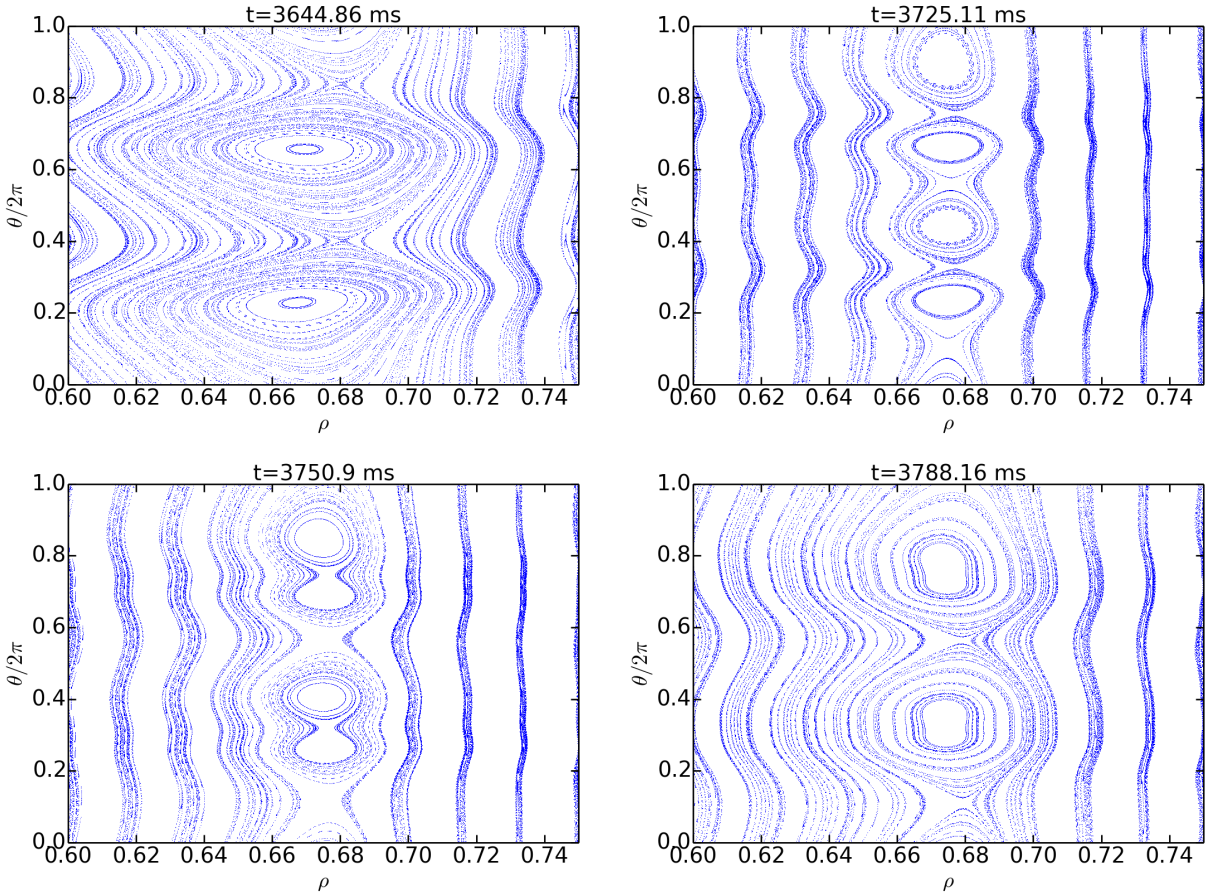

Figure 24. Poincare plots of the island at different time steps during the flip. The (2,1) structure disappears, leading to the formation of a (4,2) island whose O-points then fuse to reform a (2,1)-structure

6.3. Rotation of the source

In the simulations presented before, the island has almost zero rotation. In realistic conditions however, diamagnetic effects or momentum source, due for instance to Neutral Beam Injection, will cause the islands to rotate. Since we do not include these effects in our simulations, we emulate them by imposing the source term to rotate, defining the term ϕ_0 in equation (23) as $\phi_0 = \phi_0^0 + \omega t$ where ω is the prescribed rotation frequency ($\omega = 2\pi f$ where $f = 25$Hz). This approach is valid in the limit where we assume that the current source and the island reduction will not affect its rotation frequency. On figure 26 the evolution of the island size for a fixed 3D source, a rotating 3D source and a 1D source term is plotted. As shown in the previous section, the island under the influence of 3D localized current source "flips", while the rotating 3D source and the 1D source term do not show such behavior, and give a similar island dynamics, which is consistent with the analytical results presented in section 3.2.

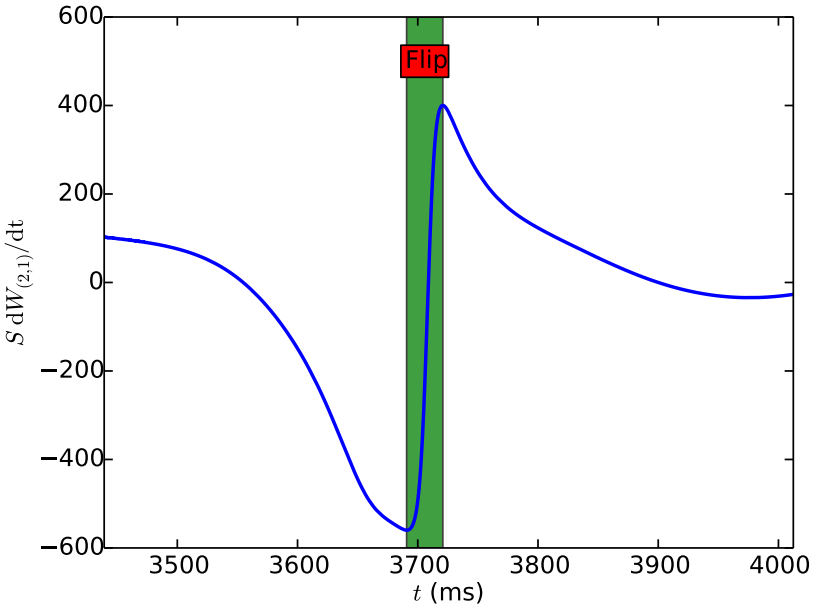

Figure 25. Evolution of the derivative of the island size with respect to the time.

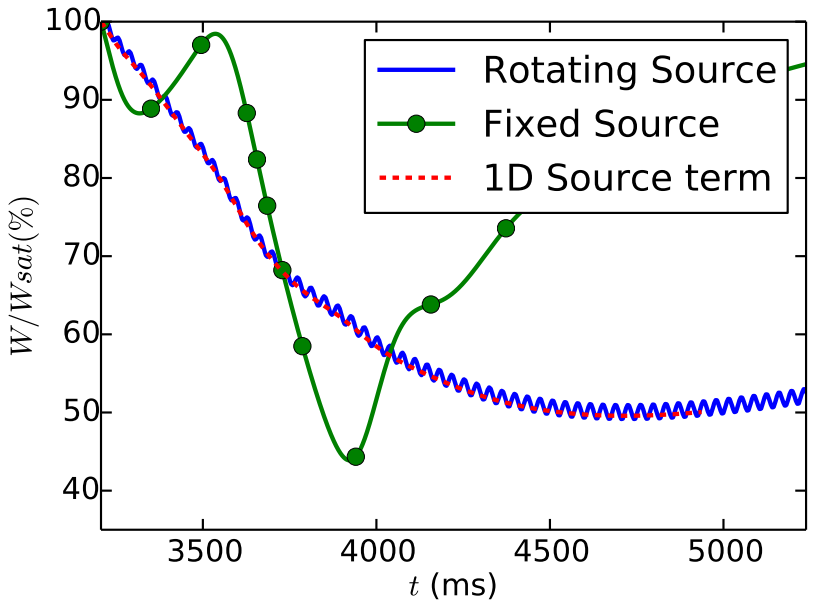

Figure 26. Evolution of the size of the $W_{(2,1)}$ island when using a fixed 3D source (no rotation) and a rotating (at $f = 25$ Hz) 3D source for $I_{RF}/I_P \approx 0.75\%$.

7. Conclusion

In this work, we reported the implementation of a current source term in view of the simulation of the island stabilization process with the code XTOR-2F. After recalling the basic principles of ECCD and presenting the model we use to homogeneize the current distribution along the field lines, we performed one-fluid MHD simulations using

an equilibrium issued from an experimental discharge on Asdex-Upgrade. Influence of parameters such as current intensity, source width and position with respect to the island have been tested and compared to the Modified Rutherford Equation. We retrieve a good agreement between the simulations and the analytical predictions concerning the variations of control efficiency with source width and position. We also show that the 3D nature of the current source term can lead to the onset of an island if the source term is precisely applied on a rational surface. We report the observation of a flip phenomenon in which the O- and X-Points of the island rapidly switch their position in order for the island to take advantage of the current drive to grow. This work opens the route to simulations of NTM stabilization with the full neoclassical model implemented in XTOR-2F [30, 31]

8. Acknowledgments

This work has been carried out within the framework of the EUROfusion Consortium and has received funding from the Euratom research and training programme 2014-2018 under grant agreement No 633053. It is part of the project AMICI granted by the Agence Nationale pour la Recherche (ANR-14-CE32-0004). This work was granted access to the HPC resources of Aix-Marseille Université financed by the project Equip@Meso (ANR-10-EQPX-29-01). A part of this work was carried out using the CURIE supercomputer, operated into the TGCC by CEA, France, in the framework of GENCI project 056348. The views and opinions expressed herein do not necessarily reflect those of the European Commission.

9. References

[1] H Zohm, G Gantenbein, F Leuterer, M Maraschek, E Poli, L Urso, and the ASDEX Upgrade Team. Control of NTMs by ECCD on ASDEX Upgrade in view of ITER application. *Plasma Physics and Controlled Fusion*, 49(12B):B341, 2007.

[2] R. J. La Haye, S. Günter, D. A. Humphreys, J. Lohr, T. C. Luce, M. E. Maraschek, C. C. Petty, R. Prater, J. T. Scoville, and E. J. Strait. Control of neoclassical tearing modes in DIII-D. volume 9, pages 2051–2060. AIP, 2002.

[3] A. Isayama, G. Matsunaga, T. Kobayashi, S. Moriyama, N. Oyama, Y. Sakamoto, T. Suzuki, H. Urano, N. Hayashi, Y. Kamada, T. Ozeki, Y. Hirano, L. Urso, H. Zohm, M. Maraschek, J. Hobirk, K. Nagasaki, and the JT-60 team. Neoclassical tearing mode control using electron cyclotron current drive and magnetic island evolution in JT-60U. *Nuclear Fusion*, 49(5):055006, 2009.

[4] F. Felici, T.P. Goodman, O. Sauter, G. Canal, S. Coda, B.P. Duval, J.X. Rossel, and the TCV Team. Integrated real-time control of MHD instabilities using multi-beam ECRH/ECCD systems on TCV. *Nuclear Fusion*, 52(7):074001, 2012.

[5] A. Pletzer and F. W. Perkins. Stabilization of neoclassical tearing modes using a continuous localized current drive. *Physics of Plasmas*, 6(5):1589–1600, 1999.

[6] C. C. Hegna and J. D. Callen. On the stabilization of neoclassical magnetohydrodynamic tearing modes using localized current drive or heating. *Physics of Plasmas*, 4(8):2940–2946, 1997.

[7] G. Kurita, T. Tuda, M. Azumi, T. Takizuka, and T. Takeda. Effect of local heating on the m=2 tearing mode in a tokamak. *Nuclear Fusion*, 34(11):1497, 1994.

[8] Q. Yu, S. Gunter, G. Giruzzi, K. Lackner, and M. Zabiego. Modeling of the stabilization of neoclassical tearing modes by localized radio frequency current drive. *Physics of Plasmas*, 7(1):312–322, 2000.

[9] A. M. Popov, R. J. La Haye, Y. Q. Liu, M. Murakami, N. N. Popova, and A. D. Turnbull. Simulation of neoclassical tearing modes in the DIII-D tokamak. II. suppression by radially localized electron cyclotron current drive. *Physics of Plasmas*, 9(10):4229–4240, 2002.

[10] Thomas G. Jenkins, Scott E. Kruger, C. C. Hegna, Dalton D. Schnack, and Carl R. Sovinec. Calculating electron cyclotron current drive stabilization of resistive tearing modes in a nonlinear magnetohydrodynamic model. *Physics of Plasmas*, 17(1):012502, 2010.

[11] D. Borgogno, L. Comisso, D. Grasso, and E. Lazzaro. Nonlinear response of magnetic islands to localized electron cyclotron current injection. *Physics of Plasmas (1994-present)*, 21(6):–, 2014.

[12] N. J. Fisch and A. H. Boozer. Creating an asymmetric plasma resistivity with waves. *Phys. Rev. Lett.*, 45:720–722, Sep 1980.

[13] E. Westerhof and J. Pratt. Closure of the single fluid magnetohydrodynamic equations in presence of electron cyclotron current drive. *Physics of Plasmas (1994-present)*, 21(10):–, 2014.

[14] R. W. Harvey, O. Sauter, R. Prater, and P. Nikkola. Radial Transport and Electron-Cyclotron-Current Drive in the TCV and DIII-D Tokamaks. *Phys. Rev. Lett.*, 88:205001, May 2002.

[15] Yves Peysson, Joan Decker, L Morini, and S Coda. RF current drive and plasma fluctuations. *Plasma Physics and Controlled Fusion*, 53(12):124028, 2011.

[16] Q. Yu, X. D. Zhang, and S. Günter. Numerical studies on the stabilization of neoclassical tearing modes by radio frequency current drive. *Physics of Plasmas*, 11(5):1960–1968, 2004.

[17] N. Bertelli and E. Westerhof. Consequences of finite transport on the effectiveness of ECCD for neoclassical tearing mode stabilization in ITER. *Nuclear Fusion*, 49(9):095018, 2009.

[18] Hinrich Lütjens, Jean-François Luciani, and Xavier Garbet. Curvature effects on the dynamics of tearing modes in tokamaks. *Physics of Plasmas*, 8(10):4267–4270, 2001.

[19] Richard Fitzpatrick. Helical temperature perturbations associated with tearing modes in tokamak plasmas. *Physics of Plasmas*, 2(3):825–838, 1995.

[20] Hinrich Lütjens and Jean-François Luciani. XTOR-2F: A fully implicit Newton-Krylov solver applied to nonlinear 3D extended MHD in tokamaks. *Journal of Computational Physics*, 229(21):8130 – 8143, 2010.

[21] A. H. Glasser, J. M. Greene, and J. L. Johnson. Resistive instabilities in general toroidal plasma configurations. *Physics of Fluids*, 18(7):875–888, 1975.

[22] Hinrich Lütjens, Jean-François Luciani, and Xavier Garbet. Nonlinear three-dimensional MHD simulations of tearing modes in tokamak plasmas. *Plasma Physics and Controlled Fusion*, 43(12A):A339–A348, 2001.

[23] D De Lazzari and E Westerhof. The role of asymmetries in the growth and suppression of neoclassical tearing modes. *Plasma Physics and Controlled Fusion*, 53(3):035020, 2011.

[24] E Lazzaro and S Nowak. ECCD control of dynamics of asymmetric magnetic islands in a sheared flow. *Plasma Physics and Controlled Fusion*, 51(3):035005, 2009.

[25] S. Nowak, E. Lazzaro, B. Esposito, G. Granucci, M. Maraschek, O. Sauter, H. Zohm, D. Brunetti, and ASDEX Upgrade Team. Interpretation of the effects of electron cyclotron power absorption in pre-disruptive tokamak discharges in asdex upgrade. *Physics of Plasmas*, 19(9):–, 2012.

[26] E. Westerhof, A. Lazaros, E. Farshi, M.R. de Baar, M.F.M. de Bock, I.G.J. Classen, R.J.E. Jaspers, G.M.D. Hogeweij, H.R. Koslowski, A. Krmer-Flecken, Y. Liang, N.J. Lopes Cardozo, and O. Zimmermann. Tearing mode stabilization by electron cyclotron resonance heating demonstrated in the TEXTOR tokamak and the implication for ITER. *Nuclear Fusion*, 47(2):85, 2007.

[27] R.J. La Haye, J.R. Ferron, D.A. Humphreys, T.C. Luce, C.C. Petty, R. Prater, E.J. Strait, and A.S. Welander. Requirements for alignment of electron cyclotron current drive for neoclassical tearing mode stabilization in ITER. *Nuclear Fusion*, 48(5):054004, 2008.

[28] R.W. Perkins, R.W. Harvey, M. Makowski, and M.N. Rosenbluth. Prospects for Electron

Cyclotron Current Drive Stabilization of Neoclassical Tearing Modes in ITER. volume 21A (Part III). 24th EPS Conference on Plasma Physics (Berchtesgaden), 1997.

[29] E. Lazzaro and M. F. F. Nave. Feedback control of rotating resistive modes. *Physics of Fluids (1958-1988)*, 31(6):1623–1629, 1988.

[30] N. Mellet, P. Maget, H. Lütjens, D. Meshcheriakov, and the Tore Supra Team. Neoclassical viscous stress tensor for non-linear MHD simulations with XTOR-2F. *Nuclear Fusion*, 53(4):043022, 2013.

[31] O. Février, P. Maget, H. Lütjens, G. Giruzzi, M. Reich, O. Sauter, P. Beyer, the ASDEX Upgrade team, and the EUROfusion MST-1 Team. Modeling of robust NTM control by ECCD in AUG. 42nd EPS Conference on Plasma Physics, Lisbon, Portugal (P1.104), 2015.